ACS Catalysis

pubs.acs.org/acscatalysis

Research Article

Actinobacterial Coproheme Decarboxylases Use Histidine as a Distal Base to Promote Compound I Formation

Hanna Michlits, Bettina Lier, Vera Pfanzagl, Kristina Djinović-Carugo, Paul G. Furtmüller, Chris Oostenbrink, Christian Obinger, and Stefan Hofbauer*

Cite This: *ACS Catal.* 2020, 10, 5405−5418

Read Online

ACCESS | Metrics & More | Article Recommendations | Supporting Information

ABSTRACT: Coproheme decarboxylases (ChdCs) catalyze the final step in heme *b* biosynthesis of monoderm and some diderm bacteria. In this reaction, coproheme is converted to heme *b* via monovinyl monopropionate deuteroheme (MMD) in two consecutive decarboxylation steps. In Firmicutes decarboxylation of propionates 2 and 4 of coproheme depend on hydrogen peroxide and the presence of a catalytic tyrosine. Here we demonstrate that ChdCs from Actinobacteria are unique in using a histidine (H118 in ChdC from *Corynebacterium diphtheriae*, *Cd*ChdC) as a distal base in addition to the redox-active tyrosine (Y135). We present the X-ray crystal structures of coproheme-*Cd*ChdC and MMD-*Cd*ChdC, which clearly show (i) differences in the active site architecture between Firmicutes and Actinobacteria and (ii) rotation of the redox-active reaction intermediate (MMD) after formation of the vinyl group at position 2. Distal H118 is shown to catalyze the heterolytic cleavage of hydrogen peroxide (k_{app} = (4.90 ± 1.25) × 10^4 M^{-1} s^{-1}). The resulting Compound I is rapidly converted to a catalytically active Compound I* (oxoiron(IV) Y135$^{\bullet}$) that initiates the radical decarboxylation reactions. As a consequence of the more efficient Compound I formation, actinobacterial ChdCs exhibit a higher catalytic efficiency in comparison to representatives from Firmicutes. On the basis of the kinetic data of wild-type *Cd*ChdC and the variants H118A, Y135A, and H118A/Y135A together with high-resolution crystal structures and molecular dynamics simulations, we present a molecular mechanism for the hydrogen peroxide dependent conversion of coproheme via MMD to heme *b* and discuss differences between ChdCs from Actinobacteria and Firmicutes.

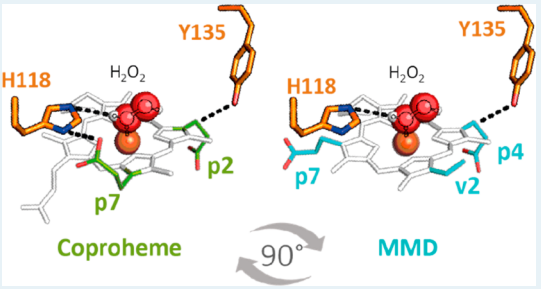

KEYWORDS: *coproheme decarboxylase, prokaryotic heme biosynthesis, enzyme kinetics, X-ray crystallography, Compound I formation*

1. INTRODUCTION

Coproheme decarboxylases (ChdCs) catalyze the ultimate step of the "coproporphyrin-dependent" heme biosynthesis pathway, which is mainly utilized in monoderm bacteria.[1−3] The product heme *b* is generated by the stepwise decarboxylation of propionate groups at positions 2 and 4 of the pyrrole rings A and B of iron coproporphyrin III (coproheme), via the three-propionate intermediate monovinyl monopropionate deuteroheme (MMD).[4,5] Coproheme and MMD are redox-active substrates.

Mechanistic studies on this reaction have mainly focused on representatives from the phylum Firmicutes, which forms a phylogenetically distinct clade (clade 1, Figure S1).[1,3] The oxidative decarboxylation of coproheme is hydrogen peroxide mediated[6] and requires 2 equiv of the oxidant for full conversion of one coproheme to heme *b*.[7] A tyrosine residue was identified as the catalytically relevant radical site essential for both decarboxylation reactions in ChdC from the Firmicutes *Staphylococcus aureus*[8] and *Listeria monocytogenes*.[9] This tyrosyl radical is formed from a Compound I (oxoiron(IV) Por$^{\bullet+}$) intermediate and manifests as Compound I*. Compound I formation was verified recently in an inactive variant of *Lm*ChdC, with chlorite as alternative oxidant.[9]

Actinobacterial representatives (clade 2, Figure S1) were highly important in the process of identifying the coproporphyrin-dependent heme biosynthesis pathway, as ChdCs from *Mycobacterium tuberculosis*, *Streptomyces coelicolor*, and *Propionibacterium acnes* were shown to be essential to form heme *b*.[4,10] However, detailed mechanistic studies on actinobacterial ChdCs are scarce. We previously demonstrated that the actinobacterial ChdC from *Corynebacterium diphtheriae* is more efficient in coproheme decarboxylation in comparison to firmicute ChdCs.[3] So far the structural basis for this drastic difference in catalytic power remains unclear. From sequence alignments and homology modeling the most striking structural difference appeared to be the length and architecture

Received: January 27, 2020
Revised: April 8, 2020
Published: April 9, 2020

Table 1. List of Primers for Cloning of *Cd*ChdC Wild-Type via Gibson Assembly into Vector pD441-NH and Variants Y135A, H118A, and H118A/Y135A (Site-Directed Mutagenesis)

		primer for Gibson assembly
wild-type (fragment 1)	forward	aattgtccttttaacagcgatcgcgtatttcgcctcgctcag
wild-type (fragment 2)	reverse	ctgagcgaggcgaaatacgcgatcgctgttaaaaggacaatt
backbone	forward	ggactggaagttctgttccaggggcccatggcagagaaattgaatttcgaag
backbone	reverse	gggcccctggaacagaacttccagtccatggtggtggtggtgatgtttcatt
		primer for site-directed mutagenesis
H118A	forward	ctgagttcaaccgcagc**gct**ctgccgtcgttcatta
H118A	reverse	taatgaacgacggcag**agc**gctgcggttgaactcag
Y135A	forward	cccgggcgattggattacggtt**gca**ccgttcgtgcgc
Y135A	reverse	gcgcacgaacgg**tgc**aaccgtaatccaatcgcccggg

of a loop close to the active site. This loop forms the substrate access channel and seems to be highly flexible in firmicute ChdCs.[2,3]

Prior to this study, only crystal structures of firmicute ChdCs were solved. Apo structures are available from *Geobacillus stearothermophilus* (*Gs*ChdC, PDB code 1T0T) and *Lm*ChdC (4WWS);[11] holo structures from *Gs*ChdC in complex with Mn-coproheme (5T2K)[12] and *Lm*ChdC in complex with iron coproheme (6FXJ) and the three-propionate intermediate (6FXQ)[9] (Figure S1). As one tyrosine is essential for both decarboxylation reactions, a single active site was identified for the oxidative decarboxylation. Therefore, the substrate needs to reorient in the active site after the first decarboxylation. This was proposed on the basis of the MMD-*Lm*ChdC crystal structure (6FXQ) and verified by extensive UV−vis and resonance Raman spectroscopic analyses of *Lm*ChdC mutants, probing the environment of all four propionate groups in the resting state[13,14] and during turnover.[9] The mechanism of hydrogen peroxide activation and Compound I formation in ChdCs from Firmicutes remains unknown, as a potential distal base for deprotonation of hydrogen peroxide is lacking.

In this study we present the first actinobacterial crystal structures of ChdC from *Corynebacterium diphtheriae* in complex with coproheme and with MMD, which prove the proposed substrate reorientation for actinobacterial representatives. Analogously to the catalytic tyrosine in Firmicutes, Y135 is shown to be essential for catalysis.[8,9,12] Most interestingly, we demonstrate—on the basis of crystal structures and UV−vis stopped-flow kinetics data—that actinobacterial ChdCs use a conserved distal histidine residue (H118 in *Cd*ChdC) as base for deprotonation and heterolytic cleavage of hydrogen peroxide. For the first time, an apparent bimolecular reaction rate for Compound I formation with the physiological oxidant hydrogen peroxide is presented. This in-depth study of wild-type *Cd*ChdC and the variants Y135A, H118A, and H118A/Y135A allows the identification of H118 as a second catalytic residue and verifies Y135 as the redox-active site. Finally we propose a molecular mechanism for the entire catalytic cycle of heme *b* formation mediated by this actinobacterial ChdC.

2. EXPERIMENTAL PROCEDURES

2.1. Expression and Purification of Wild-Type *Cd*ChdC and Variants. *Cd*ChdC gene (DIP1394) was synthesized and subcloned into a pD441-NH vector (ATUM, Newark, California) containing an N-terminal His-tag. The synthesized vector was complemented with a HRV 3C protease cleavage site between the tag and the gene of interest by overlap extension PCR. Recombinant protein production was performed in *E. coli* Tuner (DE3) (Merck/Novagen, Darmstadt, Germany) cells in LB-medium containing 100 μg mL^{-1} kanamycin. A 500 mL portion of the medium was inoculated with 1 mL of overnight culture and cultivated in shaking flasks at 37 °C and 180 rpm for 3 h. The temperature was lowered to 16 °C prior to induction with 0.5 mM isopropyl-β-D-thiogalactopyranoside (IPTG) and kept for further cultivation overnight. Cells were harvested by centrifugation (4 °C, 2700*g*, 30 min) and resuspended in 50 mL of lysis buffer (50 mM phosphate buffer pH 7.4, with 500 mM NaCl, 5% glycerol, and 0.5% Triton X-100) and lysed by three 1 min cycles of pulsed ultrasonication (1 s of sonication with 1 s between pulses, 90% power) on ice. The resulting lysate was centrifuged for 30 min at 38720*g* and 4 °C, and the supernatant was filtered (0.45 μm pore sized filter). For purification, the filtrate was loaded on a His-trap affinity column (5 mL, GE Healthcare) pre-equilibrated with binding buffer (50 mM phosphate buffer, pH 7.4, with 500 mM NaCl) on an ÄKTA system. The column was further washed with binding buffer and equilibrated with cleavage buffer (50 mM Tris-HCl with 150 mM NaCl and 1 mM EDTA). The protein was eluted with cleavage buffer after on-column cleavage from the His-tag with a likewise His-tagged HRV 3C PreScission Protease overnight at 4 °C. The eluate was concentrated using a centrifugal filter unit (Amicon Ultra-15, Merck Millipore Ltd., Tullagreen, Carrigtwohill Co. Cork, Ireland, 50 kDa cutoff) by centrifuging at 4500 *g* for 10−20 min in order to attain a volume of 1−3 mL for further purification via size exclusion chromatography (SEC) using a HiLoad 16/600 Superdex 200 pg, GE Healthcare column equilibrated with 100 mM phosphate buffer pH 7.4, with 100 mM NaCl. The collected fractions were pooled and again concentrated via a centrifugal filter unit to a concentration of 750−1000 μM. Finally, the solution was stored at −80 °C in 20 μL aliquots. *Cd*ChdC was produced in its apo form and supplemented with coproheme directly before analysis in order to avoid unintended decarboxylation activity during storage.

For crystallization and circular dichroism experiments, the enzyme was reconstituted with iron coproporphyrin III chloride (coproheme; Frontier Scientific, Logan, UT, USA) prior to SEC purification, and the SEC-purified protein was directly used for experiments. Mutants of *Cd*ChdC were produced by site-directed mutagenesis using the previously described vector as a template and expressed and purified equally (Table 1).

2.2. Coproheme Decarboxylase Activity. H_2O_2-induced conversion of supplied coproheme to MMD and heme *b* was investigated by titration of 1000 μL of the enzyme solution in

https://dx.doi.org/10.1021/acscatal.0c00411
ACS Catal. 2020, 10, 5405−5418

50 mM phosphate buffer, pH 7, with around 15 μM apoenzyme and 10 μM coproheme in a Cary 60 spectrophotometer (Agilent Technologies) with a resolution of 1.5 nm. Subequimolar amounts of H_2O_2 were added, and spectra were taken after each titration step. Samples from this solution (10 μL) were drawn and analyzed using a Dionex Ultimate 3000 system directly linked to a QTOF mass spectrometer (maXis 4G ETD, Bruker) equipped with the standard ESI source in the positive ion mode. MS scans were recorded within a range from m/z 400 to 3800, and the instrument was tuned to detect both the rather small free heme derivatives and intact proteins in a single run. For separation of the analytes a Thermo ProSwift RP-4H analytical separation column (250 × 0.200 mm) was used.

A gradient from 99% solvent A and 1% solvent B (solvent A, 0.05% trifluoroacetic acid (TFA); solvent B, 80.00% acetyl cyanide (ACN) and 20% solvent A) to 65% B in 11 min was applied, followed by a 2 min gradient from 65% B to 95% B, at a flow rate of 8 μL min^{-1} and at 65 °C. A blank run (5.0 μL of H_2O) was performed after each sample to minimize carryover effects. Relative amounts of formed MMD and heme b as well as oxidized coproheme and heme b upon addition of hydrogen peroxide were determined.

2.3. Steady-State Ligand Binding. The steady-state kinetics of cyanide binding were determined with a Cary 60 spectrophotometer (Agilent Technologies). Typically, 10 μM holo enzyme was titrated with NaCN using a DOSY titration device (DOSTAL) to a 15−20-fold excess of ligand. The absorbance change at 412/413 nm was plotted against ligand concentration and fitted in Sigma Plot with a single rectangular hyperbola with three parameters ($f = y_0 + \frac{\Delta\text{Abs} \times x}{K_D + x}$) in which y_0 is the absorbance at zero ligand concentration, ΔAbs the absorbance difference at maximum saturation, and K_D the dissociation constant.

2.4. Stopped-Flow Spectroscopy. Pre-steady-state spectroscopic changes upon addition of the oxidant H_2O_2 or the ligand NaCN were monitored using a stopped-flow apparatus equipped with a photodiode array detector (SX-18MV, Applied Photophysics). The path length and volume of the optical quartz cell were 10 mm and 20 μL, respectively. The first spectrum was taken 1 ms after mixing. All measurements were performed in 100 mM phosphate buffer, pH 7, at 25 °C. Apo *Cd*ChdC (4 μM) was reconstituted with 2 μM coproheme directly before the measurements. Oxidant/ligand concentrations were varied from 0.1 to 2 mM.

Rate constants for hydrogen peroxide mediated Compound I formation as well as cyanide binding were determined using a stopped-flow apparatus equipped with a monochromator (Pi-star, Applied Photophysics). Time traces were taken at 390/412 nm to follow the formation of Compound I/binding of cyanide. Typically, the enzyme concentration was around 2 μM and oxidant/ligand concentrations were varied from 0.1 to 1.2 mM. For the single-wavelength measurements, a minimum of three runs were performed for each ligand or substrate concentration. k_{obs} values for each substrate/ligand concentration were determined by fitting the respective time traces with a single-exponential fit ($y = a^{-k_{obs}x} + c$), in which a is the absorbance at the beginning of the reaction/ligand binding, k_{obs} is the absorbance change per second, and c is the absorbance at the end of the reaction/ligand binding. k_{obs} values were fitted using the Pro-Data viewer software and plotted against the respective oxidant/substrate concentration.

2.5. Crystallization and Structure Determination. *Cd*ChdC reconstituted with coproheme was purified by size exclusion chromatography and was stored at −80 °C for crystallization. Crystallization experiments were performed using SWISSCI 96-well 3-drop MRC crystallization plates (Molecular Dimensions, Newmarket, U.K.), adopting the vapor diffusion method. Crystallization drops were set using a Mosquito LCP (TTP Labtech, Melbourn Science Park, Melbourn, U.K.). Protein stocks were diluted in 50 mM phosphate buffer, pH 7, with or without 10 mM NaCN to a concentration of about 6.8 μg μL^{-1} as a stock for setting up crystallization plates. Seed solutions were prepared by harvesting a single drop with crystallized protein and diluting it in 50 μL of 50 mM phosphate buffer, pH 7. Ten glass beads with a diameter of 1.0 mm were added to the solution, which was vortexed for 1 min and kept on ice for 1 min; this was repeated three times. Dilutions 1:1000 in 50 mM phosphate buffer, pH 7, were used for seeding in the crystallization plates. The reservoir was filled with 40 μL of the crystallization solution. Single drops were set up with ratios of 150:200:100, 200:200:100, and 250:200:100 protein (nL):crystallization (nL):seed (nL). Crystallization plates were sealed and stored at 22 °C. Wild-type *Cd*ChdC crystallized in 16−27% PEG3500 and 0.10−0.25% $MgCl_2$. For cryoprotection, the crystallization conditions were supplemented with 25% glycerol. All crystals were harvested using cryoloops and flash-vitrified in liquid nitrogen. Data sets were collected at beamline ID-29 of the European Synchrotron Radiation Facility (Grenoble, France). Processed data sets from the EDNA[15] pipeline were used for structure refinement. The phase problem was solved by molecular replacement using Phaser-MR[16] taking PDB structure 3DTZ of putative chlorite dismutase TA0507 from *Thermoplasma acidophilum* and further by the achieved *Cd*ChdC structure described in this paper. The models were further improved by model building using maximum likelihood refinement phenix.refine and manual model building using COOT.[17,18] The phenix.french_wilson script converted intensities into amplitudes using the French and Wilson algorithm. Restraints for coproheme, MMD, and heme b (ligand ID: RM9, VOV, and FEC) were generated using eLBOW using an sdf file as input and applying the final-geometry option. Final stages of refinement included translation liberation screw (TLS) parameters with the number of TLS groups determined using phenix.tls, isotropic B-factor model, automated addition of hydrogens and water molecules, optimization of X-ray/ADP weight, and optimization of X-ray/stereochemistry weight. Figures were prepared with PYMOL (http://www.pymol.org).

2.6. Molecular Dynamics Simulations. Molecular dynamics simulations of *Cd*ChdC with coproheme and MMD as redox-active substrates, respectively, were performed using the GROMOS11[19] software for biomolecular simulation. We investigated hydrogen-bonding interactions of the redox-active substrate within the active sites and analyzed the dynamics of H118. Interactions were described by the 54a8 force field parameter set.[20] Coproheme and MMD were parametrized in analogy to heme b in the ferric form.[21] Water was modeled explicitly and described by means of the simple point charge (SPC) water model.[22] The first 10 amino acids of the N-termini of each *Cd*ChdC monomer were truncated. The initial binding poses were obtained from the respective crystal structures. MMD was additionally simulated in the coproheme position.

https://dx.doi.org/10.1021/acscatal.0c00411
ACS Catal. 2020, 10, 5405−5418

The *Cd*ChdC pentamers with the respective substrates were solvated in pre-equilibrated periodic rectangular computational boxes of SPC water with box sizes of approximately 10.2 nm × 10.4 nm × 11.0 nm. The box was cosolvated with 25 mM sodium chloride, and in order to neutralize the systems, additional sodium atoms were added (45 in the case of coproheme, 40 in the case of MMD). The simulation of one *Cd*ChdC comprises five porphyrin substrate ligands, which is comparable to five separate subunit simulations. Equations of motion were integrated using the leapfrog algorithm,[23] and bond lengths were constrained using the SHAKE algorithm,[24] which allowed for integration time steps of 2 fs. Nonbonded interactions were treated using a twin-range cutoff (short range 0.8 nm, long range 1.4 nm). For long-range interactions, a reaction field contribution with a relative dielectric permittivity of 61, as appropriate for the SPC water model, was added.[25] Initial velocities were sampled from a Maxwell−Boltzmann distribution at 60 K. The equilibration of the systems was performed by starting with a 100 ps simulation at 60 K, keeping the solutes positionally restrained by a harmonic potential with a force constant of 2.5×10^4 kJ mol^{-1}. In the subsequent equilibration steps the system was heated by 60 K in each step and the force constant was decreased by a factor of 10. The final equilibration step was conducted at 298 K for 150 ps, where position constraints were replaced by rototranslational restraints. After equilibration, production simulations were performed for 20 ns each. The temperature was maintained at 298 K by using a weak-coupling thermostat[26] of solute and solvent to two separate heat baths with a coupling time of 0.1 ps, the pressure kept constant at 1 atm with a coupling time of 0.5 ps, and an isothermal compressibility of 4.575×10^{-4} kJ nm^3. Trajectories were written every 0.2 ps. Analyses of the coordinate trajectories were performed using gromos++ programs.[27]

2.7. Assessment of Secondary Structure Integrity of *Cd*ChdC Wild-Type and Variants. In order to assess the structural integrity of the created single mutants and double mutant, electronic circular dichroism (ECD) spectra in the far (180−260 nm)- and near-UV (250−500 nm) regions were taken (Chirascan, Applied Photophysics, Leatherhead, U.K.). Conditions were as follows: spectral bandwidth, 1 nm; scan speed, 10 s nm^{-1}; path length, 1 mm; temperature, 20 °C.

Samples were prepared with 5 μg μL^{-1} (far-UV) or 10 μg μL^{-1} (near-UV) apo or coproheme bound protein in 10 mM phosphate buffer, pH 7. In order to ensure fully coproheme bound spectra, the protein was supplemented with an excess of coproheme prior to an SEC purification as described in section 2.1 before CD spectral analysis.

2.8. High-Pressure Liquid Size Exclusion Chromatography with Multiangle Light Scattering (HPLC-SEC-MALS). The homogeneity and oligomeric state of the purified proteins were determined by HPLC and size exclusion chromatography (SEC) coupled to multiangle light scattering (MALS). A LC20 prominence high-pressure liquid chromatography (HPLC) system with the refractive index detector RIF-10A, the photodiode array detector SPD-M20A (Shimadzu), and MALS Heleos Dawn8+ with QELY detector (Wyatt Technology) was used for analysis. Superdex 200 10/300 GL (GE Healthcare) was equilibrated with running buffer (phosphate buffered saline (PBS) with 200 mM NaCl (pH 7.4)). Experiments were performed at a flow rate of 0.75 mL min^{-1} and 25 °C, and the resulting data were analyzed using the ASTRA 6 software (Wyatt Technology). Proper performance of the molar mass calculation was verified by analysis of a bovine serum albumin sample. A 80 μg portion of the protein (in 5−100 μL) was loaded per run. For runs with more than one protein, 80 μg per protein was loaded. All samples were prepared in running buffer. The samples were further centrifuged (17000*g*, 10 min) and filtered through an Ultrafree-MC filter with a pore size of 0.1 μM (Merck Millipore) before loading to the column.

3. RESULTS

3.1. General Assessment of Protein Quality and Structural Integrity of Produced Wild-Type *Cd*ChdC and Variants. Wild-type *Cd*ChdC and the variants Y135A, H118A, and Y135A/H118A were obtained in highly pure form in good yield (5−10 mg L^{-1} *E. coli* culture). All four recombinant homopentameric proteins were monodisperse and eluted as single peaks in HPLC-SEC-MALS. They exhibited a wild-type-like overall secondary structure composition, as demonstrated by electronic circular dichroism (ECD) spectroscopy (Figure S2).

3.2. Structure of *Cd*ChdC. Crystal structures of *Cd*ChdC in a complex with coproheme as well as with MMD were solved at a resolution of 1.8 Å (see full statistics in Table 2). To obtain the coproheme bound structure, the crystallization solution was supplemented with cyanide in order to inhibit residual activity. In the absence of cyanide, small amounts of hydrogen peroxide present in aqueous solutions were sufficient to enzymatically decarboxylate the propionate at position 2 (p2) during the crystallization process, yielding MMD. Structures are deposited in the PDB (coproheme-ChdC, 6XUC; MMD-ChdC, 6XUB).

In the homopentameric structure the subunits are organized in a ringlike shape (Figure 1). An individual subunit comprises one C-terminal and one N-terminal ferredoxin-like domain, the latter containing the redox-active substrate (Figure 1). Direct comparison of the structure of *Cd*ChdC with that of ChdC from *Listeria monocytogenes* (*Lm*ChdC) (6FXJ) reveals a flexible loop (residues 112−125 *Cd*ChdC numbering) which is positioned close to the active site of *Cd*ChdC (Figure 2), while in *Lm*ChdC it points away from the substrate and does not contribute to the architecture of the active site.[9] Most interesting about this loop in the actinobacterial structure is the conserved (in clade 2) H118, which is located about 5 Å above the heme iron. H118 further takes part in stabilization of coproheme by establishing an H-bond to propionate at position 7 (p7) (Figure 3). With regard to the higher catalytic efficiency of *Cd*ChdC in comparison to other ChdCs,[3] this histidine is of particular interest since it could act as a distal base and contribute to deprotonation of hydrogen peroxide. It has to be mentioned that in *Lm*ChdC the flexible loop contains a histidine (H117), which is positioned at a distance of approximately 17 Å from the coproheme iron, according to structural data (6FXJ).[9] The loop position in 6FXJ is stabilized by crystal-packing contacts in two out of five subunits and most probably is a crystallographic artifact and is highly flexible in solution. The role of H117 in *Lm*ChdC and a possible movement of the loop has not yet been elucidated.

The position and orientation of coproheme in the active site is stabilized by several H-bond interactions between the propionate groups and active site residues (Figure 3). p2 forms two hydrogen bonds to R139 via one water molecule. It further interacts with R208 and T205 (mediated by water). p4 interacts with R139 as well, and in addition p4 forms H-bonds

https://dx.doi.org/10.1021/acscatal.0c00411
ACS Catal. 2020, 10, 5405−5418

Table 2. Data Collection and Refinement Statistics[a]

	coproheme-*Cd*ChdC	MMD-*Cd*ChdC
wavelength (Å)	1.0723	0.9762
resolution range (Å)	47.38−1.87 (1.94−1.87)	48.17−1.78 (1.84−1.78)
space group	$P1_21_1$	$P1_21_1$
unit cell		
a (pm)	61.02	60.97
b (pm)	123.16	123.38
c (pm)	77.89	78.01
α (deg)	90	90
β (deg)	98.4990	98.71
γ (deg)	90	90
total no. of rflns	306975 (26356)	327938 (30459)
no. of unique rflns	92358 (8365)	107260 (10074)
multiplicity	3.3 (3.1)	3.1 (2.9)
completeness (%)	98.43 (89.58)	97.87 (92.72)
mean $I/\sigma(I)$	7.67 (0.91)	7.47 (0.76)
Wilson *B* factor	30.67	28.78
R_{meas} (%)	11.29 (128.0)	10.36 (156.3)
CC1/2	99.6 (32.7)	99.6 (33.1)
no. of rflns used in refinement	92282 (8365)	106574 (10073)
no. of rflns used for R_{free}	4520 (451)	5271 (482)
R_{work}	0.1647 (0.2956)	0.1751 (0.3554)
R_{free}	0.2230 (0.3316)	0.2266 (0.3777)
no. of non-H atoms	10228	10311
macromolecules	9415	9344
ligands	245	230
solvents	568	737
no. of protein residues	1147	1142
RMS(bonds)	0.012	0.012
RMS (angles)	1.17	1.12
Ramachandran favored (%)	98.15	97.97
Ramachandran allowed (%)	1.67	1.94
Ramachandran outliers (%)	0.18	0.09
rotamer outliers (%)	0.21	0.11
clashscore	2.83	4.68
av *B* factor	39.44	40.23
macromolecules	39.51	39.78
ligands	42.25	62.72
solvent	37.07	38.98
no. of TLS groups	39	40

[a]Statistics for the highest-resolution shell are shown in parentheses.

with W143 and with E113 bridged by a water molecule. A complex hydrogen-bonding network is formed between p6 and the peptide backbone (residues 112−114). One hydrogen bond is established between p6 and N115. There are several hydrogen bonds to p7 (H118, peptide backbone 69−70).

Electron densities clearly show that MMD is positioned in a different orientation in comparison to coproheme (Figure 4). This can be seen in all five subunits of the pentameric structure. While p2 of coproheme faces the catalytic tyrosine, MMD is rotated by 90°, thereby allowing p4 to occupy this position. In MMD-ChdC only minor changes in the hydrogen-bonding network can be seen for p4 and p6 (corresponding to p2 and p4 in the coproheme structure; Figure 3). A water-mediated hydrogen bond between p6 and p7 in the coproheme structure is not present in the MMD-bound structure. The vinyl group at position 2 (v2) of MMD is in no proximity to any ligands to form noncovalent interactions.

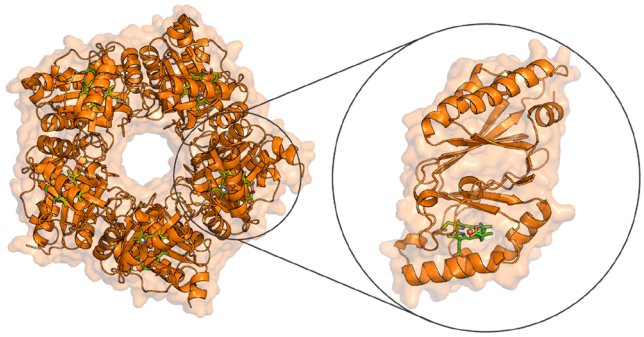

Figure 1. Overall structure of coproheme decarboxylase from *Corynebacterium diphtheriae* (*Cd*ChdC). (left) Crystal structure of pentameric *Cd*ChdC. The five subunits, each containing one coproheme, are organized in a ringlike shape. (right) One monomer is comprised of one C- and one N-terminal domain, the latter containing the substrate binding site.

3.3. Molecular Dynamics Simulations. Molecular dynamics simulations were performed in order to elucidate hydrogen-bonding interactions between the propionates and the residues in the active site. *Cd*ChdC was simulated in a complex with coproheme and MMD in the native, catalytically active poses (according to the crystal structures) or with MMD in the coproheme pose after cleavage of p2 and prior to the 90° rotation.

H-bonds involving propionates of the substrate were analyzed considering hydrogen bonds to be present if the distance between a hydrogen atom connected to a donor atom is within 0.25 nm from an acceptor and the donor−hydrogen−acceptor angle is larger than 135°. Two types of hydrogen bonds were distinguished: (i) direct hydrogen bonds (solute−solute bonds) between propionates of the substrates and amino acid residues and (ii) bridging hydrogen bonds (solute−solvent−solute bridges), where a water molecule facilitates the hydrogen bonding. In Table 3 the mean number of H-bonds over a 20 ns simulation time averaged over the five monomers per propionate and residue are given. H-bonds were considered for residues with the occurrence of more than 0.01 H-bond per residue. In addition, the sums of direct H-bonds and bridging H-bonds per propionate, per substrate, and the total sums are included in Table 3. The total H-bond occurrence is highest for the coproheme substrate, mainly because of its four propionate groups and thus more hydrogen bond acceptors. After cleavage of the p2 carboxylic group, the MMD in the coproheme pose forms similar hydrogen bonds. The maximum difference is observed with p4, which interacts more strongly in the simulations of the three-propionate intermediate. The H-bond occurrence of MMD after rotation (pose that corresponds to the crystal structure) is higher than that in the initial pose. The residues with the most interactions are R139 and W143 in both poses, but the interactions are facilitated through p4 and p6, respectively. The H-bonding interactions suggest that the MMD pose after rotation is slightly more favorable.

The flexibility of H118 was evaluated by analyzing the distance of the *δ* nitrogens to the iron centers of the substrates. The distance−time series for the five subunits of the three different systems coproheme (native pose) and MMD (native and coproheme poses) were generated (Figure 5). The normalized densities of the distances from the *δ* nitrogen of H118 to the iron in nanometers are plotted for the five

https://dx.doi.org/10.1021/acscatal.0c00411
ACS Catal. 2020, 10, 5405−5418

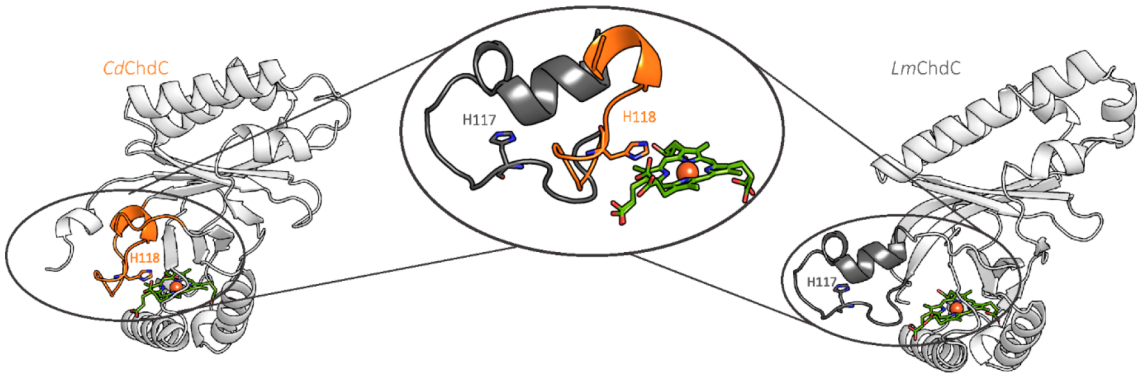

Figure 2. Differences in structure of loop 112−115 (*Cd*ChdC numbering) between Actinobacterial and Firmicutes ChdCs: (left) *Cd*ChdC; (right) ChdC from *Listeria monocytogenes* (*Lm*ChdC). (center) Overlay of the flexible loop of *Cd*ChdC (orange) and LmChdC (gray) depicts the difference in length and orientation. H118 in *Cd*ChdC and H117 in *Lm*ChdC are shown in stick representation.

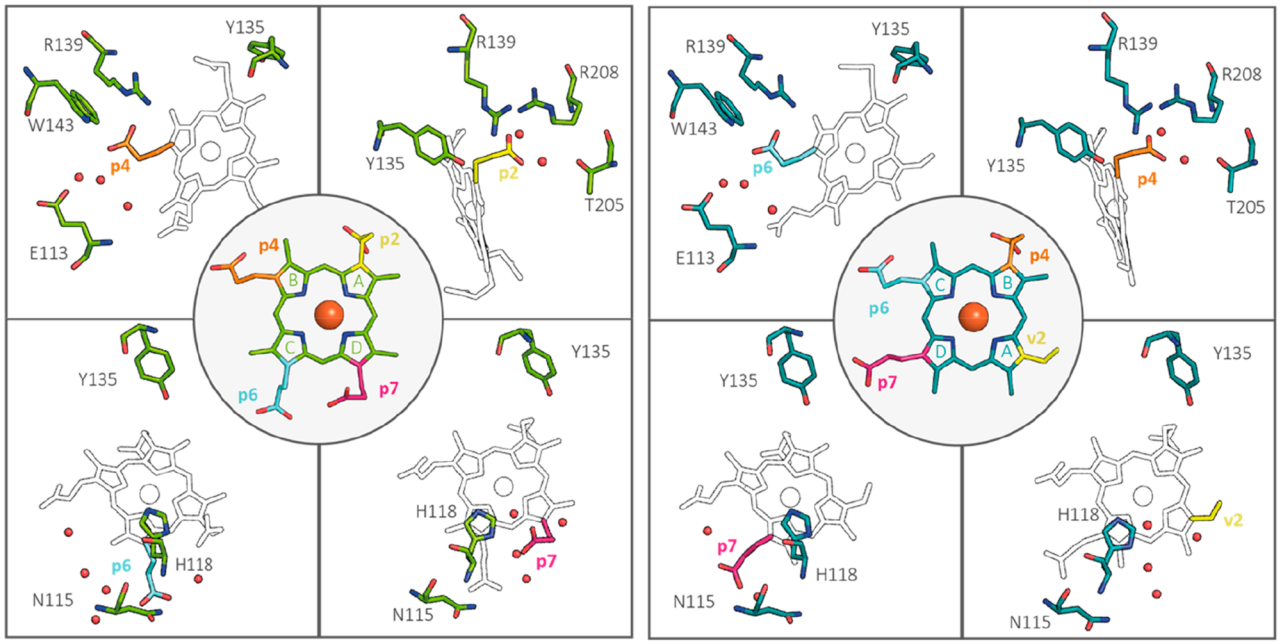

Figure 3. Noncovalent interactions of coproheme and monovinyl monopropionate deteroheme (MMD) in *Cd*ChdC. (left) Carbon atoms of amino acid residues involved in interactions with coproheme (crystal structure of coproheme-*Cd*ChdC) are shown as green sticks. Water molecules are shown as red spheres. The color code of carbon atoms of propionates p2, p4, p6, and p7 in coproheme is depicted in the middle subpanel and corresponds to that of Table 3. (right) Carbon atoms of amino acid residues involved in interactions with MMD (crystal structure of MMD-*Cd*ChdC) are shown as blue sticks. The color code of vinyl and propionates v2, p4, p6, and p7 in coproheme is depicted in the middle subpanel and corresponds to that of Table 3 (p2, v2, yellow; p4, orange; p6, cyan; p7: magenta).

individual subunits of the three systems (Figure 5). Pronounced peaks are observed at a distance of 0.43 nm, especially for coproheme in its native position and MMD in the coproheme pose. This indicates a relatively low flexibility of the histidine residue. In the MMD simulation (native pose) just one subunit shows this behavior. In the coproheme simulation, two subunits show a slightly higher flexibility. The H118 residues in the MMD simulation are fluctuating with maximum distances of up to 1.6 nm; the normalized densities are much broader and spread toward higher distances (Figure 5).

The differences in flexibility of H118 can also be deduced from an H-bond analysis. It interacts quite strongly with coproheme and MMD in the coproheme pose, forming an average of one hydrogen bond with p7 over the complete trajectory when direct and bridging H-bonds are added up. With MMD in its catalytically active pose, p7 adapts a completely different position due to the 90° rotation and interacts with fewer than 0.1 H-bonds on average.

3.4. Coproheme Decarboxylase Activity. Next we investigated the influence of Y135 and H118 on the decarboxylase activity of *Cd*ChdC by exchanging the respective amino acids with alanine. The coproheme complexes of wild-type *Cd*ChdC and the variants Y135A and H118A were titrated with hydrogen peroxide in order to follow the stepwise decarboxylation from coproheme via MMD to heme *b* by UV−vis spectroscopy and mass spectrometry (Figures 6A,B).

High-spin wild-type coproheme *Cd*ChdC shows a Soret maximum at 392 nm (ε_{392} = 68000 M^{-1} cm^{-1}) and a shoulder at around 387 nm as well as Q and charge transfer bands (CT) at 497 and 635 nm, respectively. Upon addition of H_2O_2, coproheme *Cd*ChdC is converted to heme *b* *Cd*ChdC with a

https://dx.doi.org/10.1021/acscatal.0c00411
ACS Catal. 2020, 10, 5405−5418

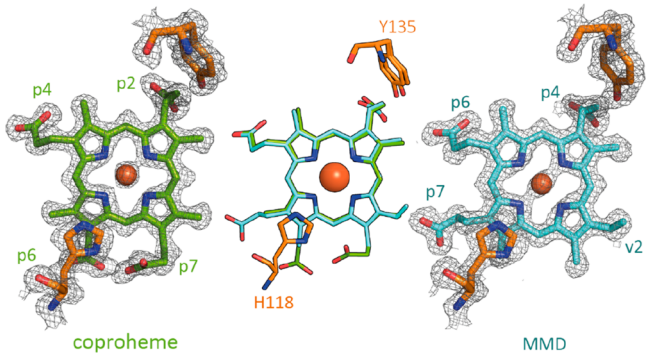

Figure 4. Orientation of coproheme and MMD in *Cd*ChdC. The crystal structure of *Cd*ChdC in a complex with carbon atoms of coproheme in green (6XUC) and carbon atoms of MMD in cyan (6XUB) clearly show a reorientation of the three-propionate reaction intermediate (MMD) after conversion of propionate at position 2 (p2) to vinyl (v2). $2|F_o| - |F_c|$ electron density maps are shown at σ = 1.5 of chain A of the respective structures.

Soret maximum at 404 nm, Q bands at 498 and 531 nm, and a CT band at 640 nm.

The inactive coproheme complex of Y135A exhibits wild-type-like spectral properties, including the extinction coefficient of the Soret maximum. Upon addition of H_2O_2, a decrease of absorbance in the Soret maximum is observed without a concomitant red shift. In addition, a prominent peak at 580 nm appears.

The spectrum of H118A differs from that of the wild-type enzyme. Its Soret maximum is red-shifted to 398 nm and is sharper (ε_{398} = 120000 M^{-1} cm^{-1}), whereas Q and CT bands are slightly blue shifted to 494 and 612 nm, respectively. The resulting spectrum after addition of a 3-fold excess of hydrogen peroxide resembles that of the wild-type enzyme with a Soret maximum at 404 nm, Q bands at 498 and 531 nm (shoulder), a weak band at 587 nm, and the CT band at 640 nm.

Insets to Figure 6A show the decrease in absorbance at the Soret maximum of coproheme and the increase of the red-shifted Soret maximum of heme *b* upon addition of H_2O_2 to the wild-type enzyme and the mutants. Wild-type *Cd*ChdC reaches a plateau after addition of a 2-fold excess of hydrogen peroxide, whereas in Y135A only a decrease in absorbance was observed due to coproheme bleaching by the oxidant. In the variant H118A the absorbance at 404 nm increases until addition of a 1.5-fold excess of hydrogen peroxide but finally

Table 3. Hydrogen-Bonding Interactions between Substrate-Propionates and Amino Acid Residues in the Active Site of *Cd*ChdC for the Three Simulated Systems: i.e., Coproheme in the Resting State, MMD (Monovinyl Monopropionyl Deuteroheme) in Coproheme Pose, and MMD in Catalytically Active Pose (90° Rotation)[a]

direct HB	coproheme				MMD in coproheme pose				MMD			
	p2	p4	p6	p7	v2	p4	p6	p7	v2	p4	p6	p7
E113												
N115			0.84	0.11			0.82					0.52
H118				0.70				0.57				0.05
R139(NE)		0.52				0.08					0.37	
R139(ND)	0.38	0.12				0.35					0.28	
W143		0.88				0.72					0.74	
T205												
R208	0.67									0.58		
	1.05	1.52	0.84	0.81		1.15	0.82	0.57		0.58	1.39	0.57
sum direct	4.22				2.53				2.54			

bridging HB	coproheme				MMD in coproheme pose				MMD			
	p2	p4	p6	p7	v2	p4	p6	p7	v2	p4	p6	p7
E113		0.63				0.62					0.45	
N115			0.11	0.20			0.19					0.05
H118				0.35				0.41				0.04
R139(NE)												
R139(ND)	0.75	0.41				0.98				1.08	0.64	
W143		0.38				0.89					0.74	
T205	0.76									0.42		
R208	0.18									0.39		
	1.69	1.42	0.11	0.55		2.48	0.19	0.41		1.89	1.83	0.09
sum bridging	3.77				3.09				3.81			
sum total	**7.99**				**5.62**				**6.35**			

[a]Direct and bridging hydrogen bonds are given separately.

https://dx.doi.org/10.1021/acscatal.0c00411
ACS Catal. 2020, 10, 5405−5418

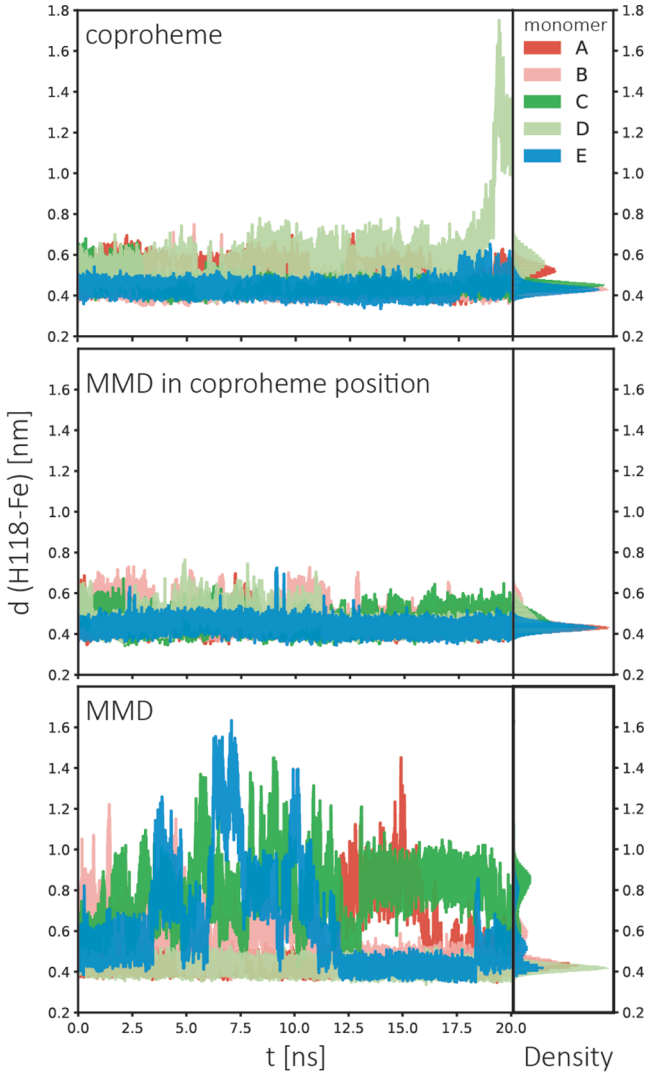

Figure 5. Flexibility of H118 in coproheme *Cd*ChdC and MMD *Cd*ChdC. Distance analysis of the three simulated systems: i.e., coproheme in the resting state, MMD in the coproheme pose, and MMD in the catalytically active pose (90° rotation). The normalized densities for the distances (in nanometers) of the δ nitrogen of H118 to the iron centers of the substrates of the individual monomers are plotted.

decreases at higher hydrogen peroxide to protein ratios, indicating bleaching of the redox-active substrate.

The ratios of heme species present in the respective reaction mix determined by mass spectrometry show that, in wild-type *Cd*ChdC and the H118A variant, addition of equimolar amounts of H_2O_2 leads primarily to formation of MMD (662.2 Da), while only minor amounts of the final product heme *b* (616.2 Da) are formed (Figure 6B). Further addition of the oxidant leads to conversion to heme *b*, which is predominant in the wild-type enzyme (~75%) but <50% in H118A. In fact, in the H118A variant oxidized heme *b* (632.2 Da) is detected after addition of a 3-fold excess of hydrogen peroxide, while minor amounts of the substrate coproheme (708.2 Da) are still present. No oxidized three-propionate intermediate was detected in any analysis.

Exchange of the catalytic Y135 by alanine leads to complete loss of decarboxylation activity. Upon addition of hydrogen peroxide, only oxidation of coproheme (724.2 Da) was detectable by mass spectrometry. The chemical and electronic structures of the oxidized coproheme species in Y135A are unknown and need to be investigated in future studies.

Kinetic studies monitoring the change in absorbance at 412 nm as a readout for heme *b* formation allowed direct comparison of the enzymatic activity of wild-type *Cd*ChdC and the variants H118A and Y135A (Figure 6C). With wild-type *Cd*ChdC the reaction is complete within a few seconds (3−5 s), whereas with H118A it takes approximately 10 times longer (>40 s). No change in absorbance is observed with Y135A in the same experimental setup.

3.5. Histidine 118 Promotes Heterolytic Cleavage of Hydrogen Peroxide. It has been postulated that a catalytically active Compound I* (oxoiron(IV) Y$^{\bullet}$), which attacks p2 in coproheme ChdC and p4 in MMD ChdC, is rapidly formed by electron transfer from the catalytic tyrosine to Compound I (oxoiron(IV) porphyryl radical).[8,9] As a consequence, ChdC Compound I can only be trapped kinetically in the absence of the redox-active tyrosine (Y135 in *Cd*ChdC). In order to assess whether H118 is involved in the catalysis of Compound I formation in actinobacterial *Cd*ChdC, we have studied the wild-type protein and the variants Y135A and H118A/Y135A by stopped-flow spectroscopy (Figure 7).

Despite the fact that upon reaction of wild-type *Cd*ChdC with hydrogen peroxide multiple spectral species are observed, it is possible to trace the formation of Compound I by a single-exponential fit of the initial rapid decrease of absorbance of the Soret maximum (k_{app} = (4.90 ± 1.25) × 10^4 M^{-1} s^{-1}). The high *y* intercept is caused by further competing reactions after Compound I formation. A red shift is already observed after 0.07 s (Figure 7A, dark green trace, partially Compound I) due to the decarboxylation reaction following Compound I formation. The resulting intermediate spectrum has its Soret maximum at 414 nm and bands at 532 and 551 nm (Figure 7A, cyan trace). After 23.63 s a heme *b* like spectrum (407, 538, and 581 nm) has evolved.

Upon mixing of the variant Y135A with hydrogen peroxide, formation of Compound I is observed with hypochromicity at the Soret maximum at 392 nm and prominent bands at 536, 583, and 645 nm (Figure 7B). During spectral conversion, clear isosbestic points at 345, 435, and 550 nm are observed. The time traces at 390 nm were monophasic, and k_{obs} values were calculated from single-exponential fits. From the plot of k_{obs} values versus H_2O_2 concentration an apparent bimolecular rate constant (k_{app}) was calculated to be (1.45 ± 0.21) × 10^4 M^{-1} s^{-1} (Table 4).

In order to evaluate the role of H118 in Compound I formation, we have designed the double variant H118A/Y135A (Figure 7C). Upon its reaction with H_2O_2 a less pronounced Compound I spectrum is observed in comparison to *Cd*ChdC Y135A with a red-shifted Soret maximum at 397 nm and bands at 541, 573, and 628 nm. During spectral conversion isosbestic points at 345, 420, 462, and 539 nm are observed. The initial time traces monitored at 390 nm are monophasic and were fitted by single-exponential means, allowing calculation of k_{app} = 6.3 × 10^2 M^{-1} s^{-1}, which is about 2 orders of magnitude slower in comparison to Compound I formation in wild-type *Cd*ChdC and Y135A.

3.6. Cyanide Binding. To assess the accessibility of the coproheme iron as well as to mirror Compound I formation, cyanide binding was studied kinetically by conventional stopped-flow spectroscopy as well as thermodynamically by spectrophotometric titration. Figure 8A shows the spectral

https://dx.doi.org/10.1021/acscatal.0c00411
ACS Catal. 2020, 10, 5405−5418

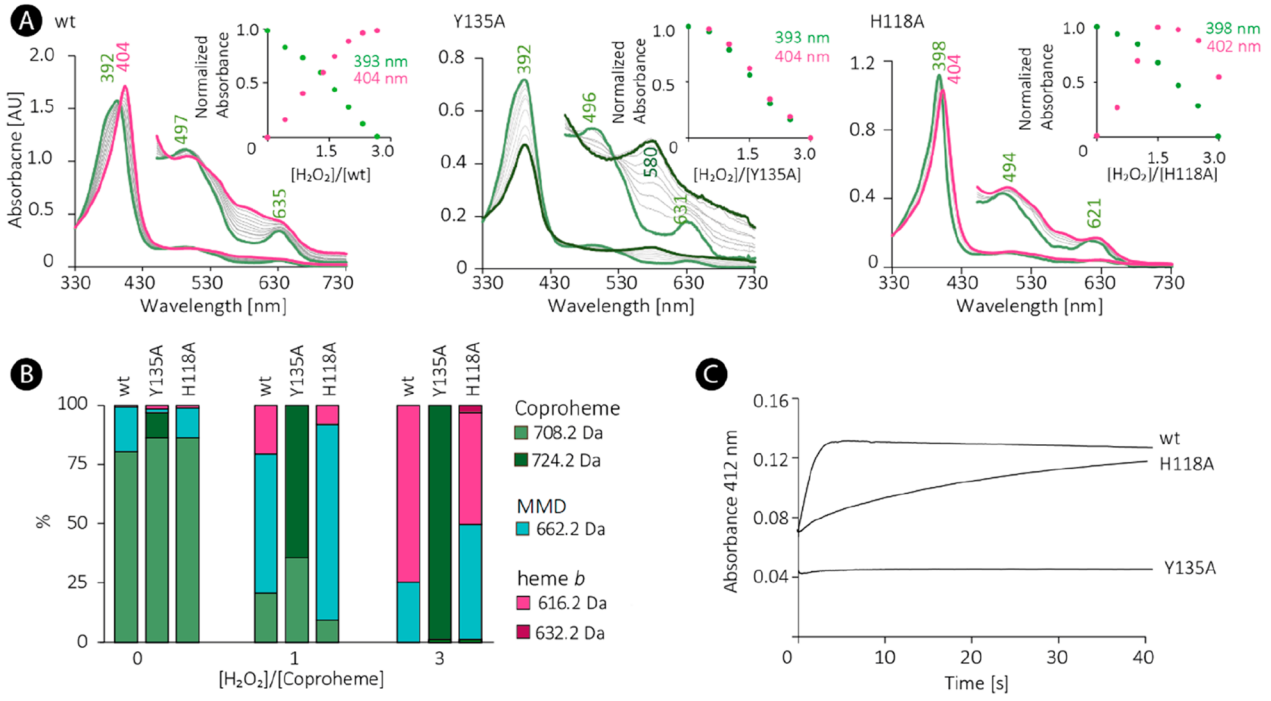

Figure 6. Activity of wild-type coproheme decarboxylase (*Cd*ChdC) and the variants Y135A and H118A followed by UV−vis spectroscopy and mass spectrometry. (A) Spectral transition upon mixing of 10 μM wild-type (wt), Y135A, and H118A *Cd*ChdC with hydrogen peroxide up to 30 μM. Spectra of the coproheme bound proteins are shown in light green. (B) Mass spectrometric analysis of the same reaction mix from (A) showing the ratios of heme species present in the reaction mix. (C) Time traces of 2 μM wt, H118A, and Y135A *Cd*ChdC with 50 μM H_2O_2 followed at 412 nm.

conversion of five-coordinated high-spin (5cHS) wild-type coproheme *Cd*ChdC to the six-coordinated low-spin (6cLS) cyanide coproheme complex, which includes a shift of the Soret maximum from 392 to 410 nm and of the Q band from 498 to 534 nm. Similar spectral transitions can be seen in the mutants. The absorbance changes at 412 nm were fitted by single-exponential calculations, and k_{obs} values were plotted against cyanide concentrations in order to determine k_{on} from the slope of the plot and k_{off} from the y intercept. Calculated k_{on} and k_{off} values are within (1.3−5.1) × 10^3 and 0.049−0.129 M^{-1} s^{-1} for all studied proteins (Table 5). The calculated K_D values for wild-type *Cd*ChdC (20.7 μM), Y135A (52.5 μM), H118A (27.5 μM), and the double variant H118A/Y135A (99.2 μM) are similar to those calculated from the hyperbolic fits ($f = y_0 + \frac{\Delta Abs \times x}{K_D + x}$) of the respective titration experiments: i.e., wild-type *Cd*ChdC (29.1 μM), Y135A (39.8 μM), H118A (36.4 μM), and the double variant H118A/Y135A (100.4 μM) (Figure 8B and Table 5).

4. DISCUSSION

Recent kinetic data have demonstrated that actinobacterial (clade 2) *Cd*ChdC is a better catalyst for conversion of coproheme to heme *b* in comparison to ChdCs from Firmicutes (clade 1, Figure S1).[3] The experimental data presented in this work provide the explanation for its higher catalytic power. This allows us to present a mechanistic model of the entire reaction cycle of actinobacterial coproheme decarboxylases.

Preceding studies on ChdCs from Firmicutes provided the first results on the biochemical mechanism of coproheme decarboxylation.[8,9,12] They demonstrated that the reaction strictly depends on (i) hydrogen peroxide, (ii) a redox-active ferric substrate (coproheme or MMD), and (iii) the presence of a catalytic redox-active (conserved) tyrosine residue. Apo-ChdC has been shown to rapidly bind the substrate coproheme, whose redox-active nature is required for the reaction.[28] It has been proposed that H_2O_2 oxidizes coproheme/MMD to a Compound I like species similar to Compound I formation in heme peroxidases and catalases. However, so far it has been impossible to trap this redox intermediate using the physiological oxidant H_2O_2.[9] The proposed Compound I like intermediate was suggested to be immediately converted to Compound I* by internal quenching of the porphyryl radical and formation of a distinct oxidized catalytic tyrosine (Y135 in *Cd*ChdC).[8,9] The neutral tyrosyl radical abstracts a hydrogen atom from the β carbon of p2, followed by migration of the unpaired propionyl electron to the substrate and reduction of the oxoiron(IV) species to the ferric state. Concomitantly the substituent is stabilized by elimination of carbon dioxide, thereby forming the vinyl substituent at position 2 (v2).[9] The resulting MMD is proposed to rotate by 90° in order to form the catalytically active MMD-ChdC with p4 in close vicinity to catalytic tyrosine. After formation of MMD-Compound I and MMD-Compound I* mediated by another hydrogen peroxide molecule, p4 is attacked by the tyrosyl radical and the second decarboxylation reaction follows the sequence as described above.

So far, spectral observations of Compound I in firmicute ChdCs have only been reported with the inactive *Lm*ChdC variant Y147A in reaction with chlorite.[9] Rate constants were determined to be in the range of 10^4 M^{-1} s^{-1}. It has to be noted that, in contrast to the natural substrate hydrogen

https://dx.doi.org/10.1021/acscatal.0c00411
ACS Catal. 2020, 10, 5405−5418

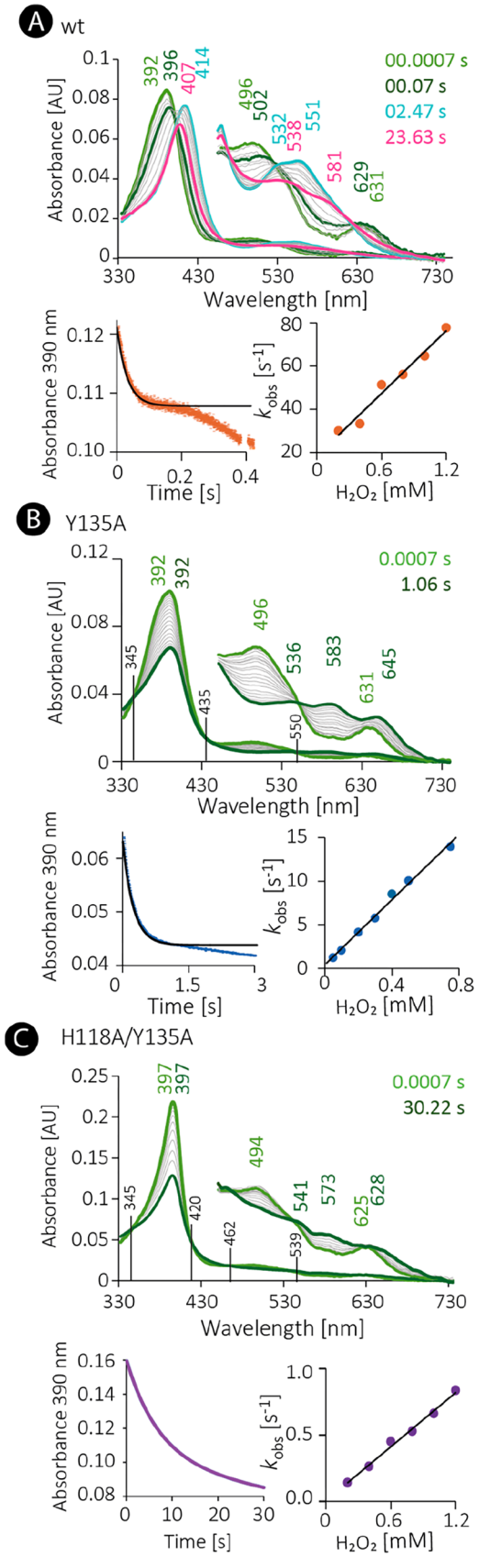

Figure 7. Kinetics of Compound I formation of wild-type *Cd*ChdC and variants. Spectral transition upon mixing of 2 μM wild-type (wt) *Cd*ChdC (A), Y135A (B), or H118A/Y135A (C) with 200 μM H_2O_2 in 50 mM phosphate buffer, pH 7.0. Initial spectra depicting the coproheme ferric resting state are shown in light green, and spectra of

Figure 7. continued

prominent intermediates are highlighted. In addition, representative monophasic time traces at 390 nm and single-exponential fits are shown together with linear plots of calculated k_{obs} values versus hydrogen peroxide concentration.

Table 4. Apparent Bimolecular Rate Constants for Hydrogen Peroxide-Mediated Compound I Formation of Wild-Type *Cd*ChdC and the Variants Y135A and H118A/Y135A at pH 7 and 25 °C

	k_{app} (M^{-1} s^{-1})
*Cd*ChdC wild-type	$(4.90 \pm 1.25) \times 10^4$
*Cd*ChdC Y135A	$(1.45 \pm 0.21) \times 10^4$
*Cd*ChdC H118A/Y135A	$(6.30 \pm 0.02) \times 10^2$

peroxide, Compound I formation with chlorite at pH 7.0 does not require deprotonation of the oxidant (pK_a of chlorite is 1.97). In Firmicutes a potential distal base for deprotonation of H_2O_2, which is required for efficient formation of Compound 0 (Fe(III)-$^-$OOH) has not yet been identified. In *Cd*ChdC Y135A we were able to detect an explicit, fully established electronic absorbance Compound I spectrum in reaction with the natural substrate H_2O_2. We could determine apparent rate constants for the initial reaction step for the inactive variant Y135A ($(1.45 \pm 2.10) \times 10^4$ M^{-1} s^{-1}) as well as the wild-type ($(4.9 \pm 1.25) \times 10^4$ M^{-1} s^{-1}; Figure 7B). The higher catalytic efficiency with a protonated oxidant indicates the presence of a distal base in this actinobacterial enzyme.

Thus, the distal histidine (H118), discovered in the crystal structure of *Cd*ChdC (Figure 3), is positioned at an optimal distance from the coproheme iron (~5 Å) and may act as the Lewis base for Compound 0 formation. This histidine is situated on the flexible loop previously shown to define the substrate channel in ChdCs (Figure 2).[3] In the well-studied firmicute *Lm*ChdC the loop points away from the coproheme cavity and the position of H118 in *Cd*ChdC remains vacant. Importantly, a previously reported I-TASSER model of *Cd*ChdC predicted an alternate loop conformation which rendered identification of H118 as a distal base almost impossible (Figure S3). However, the different orientation of the loop does not influence the accessibility of the porphyrin iron, as shown by the similar kinetics of cyanide binding (Table 5 and Figure 8).[11,28]

Compound I formation of an inactive Y135A variant lacking H118 is 2 orders of magnitude slower in comparison to wild-type *Cd*ChdC. The decreased k_{app} of Compound I formation of H118A/Y135A is comparable to coproheme conversion rates in *Lm*ChdC (1.8×10^2 M^{-1} s^{-1})[7] and *Staphylococcus aureus* ChdC (*Sa*ChdC), where a k_{obs} value of 0.3 min^{-1} was determined with 60 μM hydrogen peroxide, which corresponds to approximately 0.8×10^2 M^{-1} s^{-1}.[6] This suggests that in firmicute ChdCs uncatalyzed Compound I formation represents the rate-limiting step in the overall coproheme decarboxylation cycle.

Despite the presence of the distal catalytic histidine, Compound I formation in *Cd*ChdC is about 3 orders of magnitude slower in comparison to conventional heme peroxidases that typically use a distal histidine−arginine pair for efficient catalysis of heterolytic cleavage of hydrogen peroxide. For example, in horseradish peroxidase (HRP) Compound I formation occurs at a rate of 1.7×10^7 M^{-1} s^{-1} [29]

https://dx.doi.org/10.1021/acscatal.0c00411
ACS Catal. 2020, 10, 5405−5418

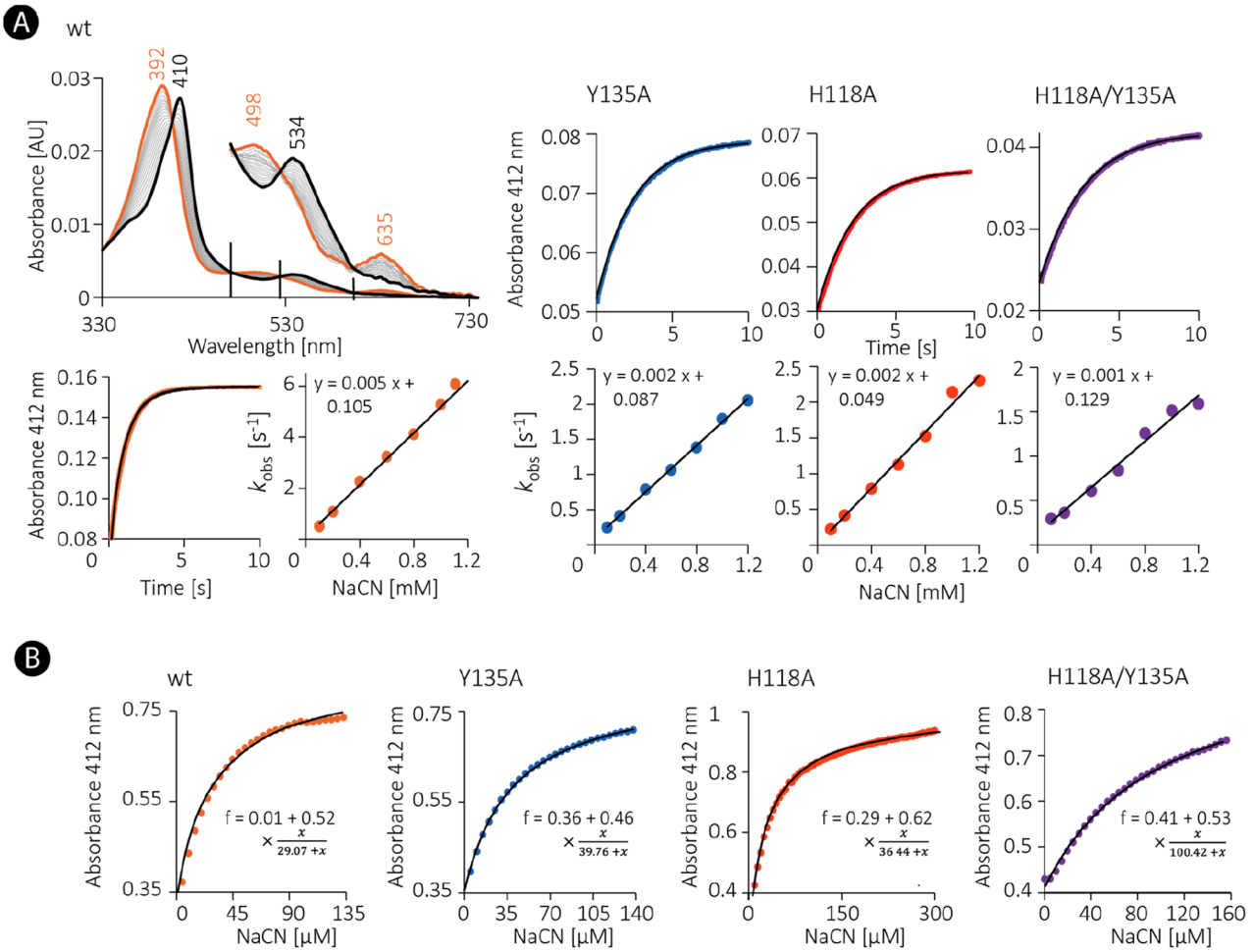

Figure 8. Kinetics and thermodynamics of cyanide binding to wild-type *Cd*ChdC and variants. (A) Kinetics of spectral transition of reaction between wild-type *Cd*ChdC (2 μM) and sodium cyanide (200 μM) in 50 mM phosphate buffer pH 7. The first spectrum (1 ms) is highlighted in orange, the 6cLS spectrum after 1.679 s in black, and intermediate spectra in gray. Typical time traces at 412 nm as well as linear plots of calculated k_{obs} values versus cyanide concentrations are shown for wild-type *Cd*ChdC (orange), Y135A (blue), H118A (red), and H118A/Y135A (purple), respectively. (B) Titration of cyanide to wild-type *Cd*ChdC (orange), Y135A (blue), H118A (red), and H118A/Y135A (purple), respectively, followed at 412 nm.

Table 5. Kinetics and Thermodynamics of Cyanide Complex Formation of Wild-Type *Cd*ChdC and the Variants H118A, Y135A, and H118A/Y135A[a]

	k_{on} (10^3 M^{-1} s^{-1})	k_{off} (s^{-1})	K_D (μM) (=k_{off}/k_{on})	K_D (μM)
*Cd*ChdC wild-type	5.1	0.105	20.7	29.1
*Cd*ChdC Y135A	1.7	0.087	52.5	39.8
*Cd*ChdC H118A	1.8	0.049	27.5	36.4
*Cd*ChdC H118A/Y135A	1.3	0.129	99.2	100.4

[a]The kinetic rate constants k_{on} and k_{off} are derived from conventional stopped-flow experiments with $K_D = k_{off}/k_{on}$ (pH 7.0, 25 °C). The K_D values derived from titration experiments (end-point titration) are given.

and follows the classical Poulos–Kraut mechanism.[30,31] In HRP the distal arginine residue promotes polarization of the oxygen–oxygen bond, thereby facilitating heterolytic cleavage.[31] A comparable positively charged interaction partner for H118 is missing in *Cd*ChdC, which may well explain the slower rate.

The significantly higher reactivity of *Cd*ChdC toward H_2O_2 in comparison to *Lm*ChdC described above was evidenced by reaction with very small amounts of hydrogen peroxide present in aerated aqueous buffer solutions that led to formation of MMD even in the absence of intentionally added H_2O_2. This allowed us to obtain the structure of pure MMD-*Cd*ChdC (PDB code: 6XUB) in addition to the crystal structure of coproheme-*Cd*ChdC (PDB code: 6XUC). The position and number of the respective propionate (and vinyl) groups are clearly visible in four out of five subunits in both structures. This strongly suggests reorientation of MMD after conversion of p2 to v2 (Figures 2, 3, and 9). The two independent, well distinguishable structures confirm what has been recently indicated in a single data set collected from *Lm*ChdC, in which partial conversion of coproheme to MMD was proposed and considered in structure refinement, finally leading to better statistics.[9] The favorability of the rotated and catalytically active position of MMD (which brings p4 in close vicinity to the catalytic tyrosine) is supported by MD simulations and quantification of hydrogen bonds established between coproheme *Cd*ChdC and *Cd*ChdC in complex with MMD in

https://dx.doi.org/10.1021/acscatal.0c00411
ACS Catal. 2020, 10, 5405–5418

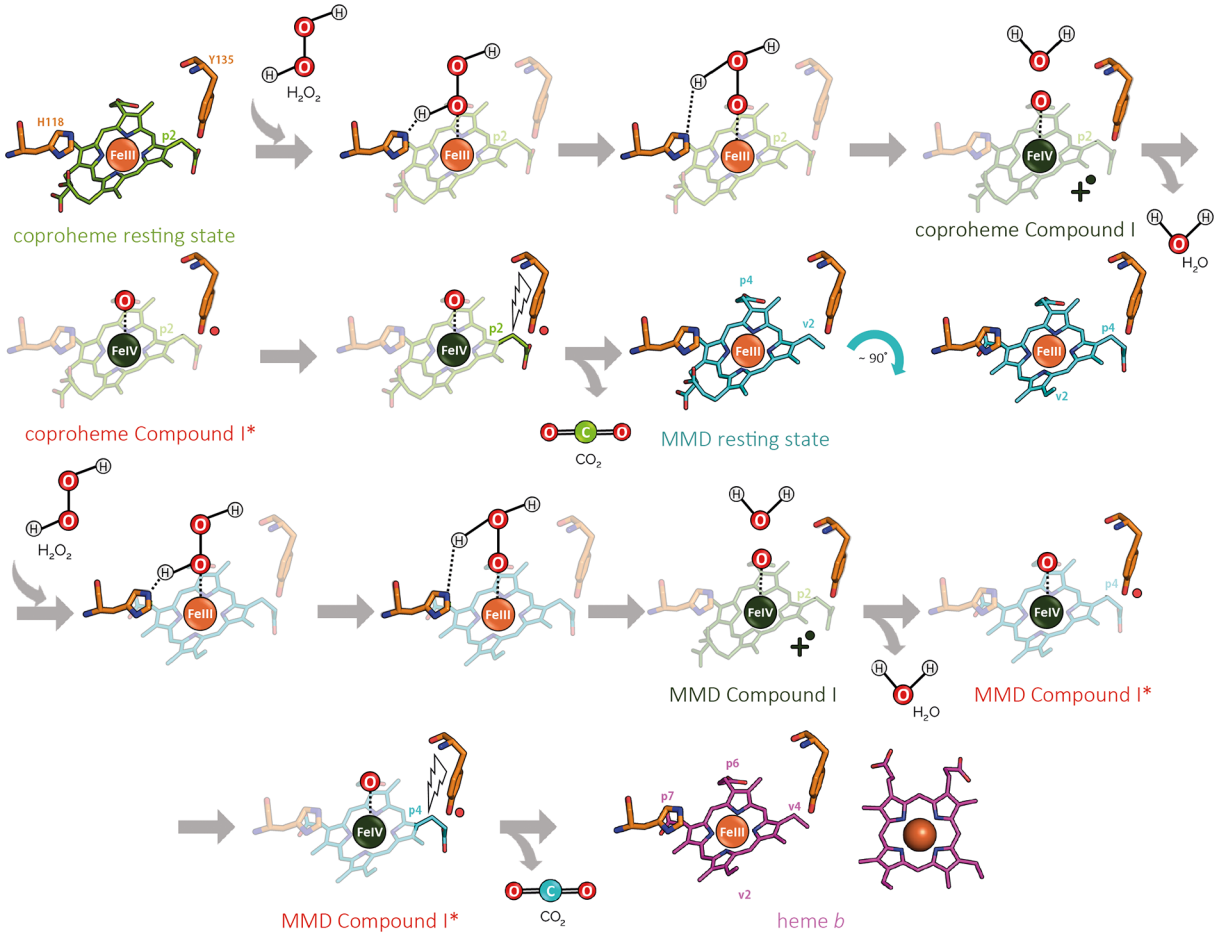

Figure 9. Complete catalytic cycle of coproheme decarboxylation in actinobacterial *Cd*ChdC. The reaction cycle starts with oxidation of the ferric resting state of coproheme *Cd*ChdC by hydrogen peroxide to Compound I (oxoiron(IV) porphyryl radical) and water. Histidine 118 acts as a distal base and promotes heterolytic cleavage of H_2O_2. Compound I is rapidly converted to Compound I* (oxoiron(IV) Y135$^{\bullet}$) by internal electron transfer. The neutral tyrosine radical performs a nucleophilic attack on the β carbon of propionate at position 2 (p2), thereby initiating its decarboxylation and formation of vinyl (v2). The resulting monovinyl monopropionate deuteroheme (MMD) undergoes a rotation of approximately 90°, thereby moving p4 in the position close to Y135. The second half of the reaction cycle starts with oxidation of the ferric resting state of MMD *Cd*ChdC by hydrogen peroxide to MMD-Compound I which is rapidly converted to MMD-Compound I* that attacks p4, thereby initiating its decarboxylation and formation of vinyl (v4). Finally, heme *b* is released and delivered to proteins.

its initial and rotated poses (Table 3). The overall amount of noncovalent interactions between MMD and nearby amino acids is slightly higher in the catalytically active pose.

Not only time-resolved spectroscopic and mass spectrometric data of *Cd*ChdC but also data obtained from representatives of Firmicutes suggest that the first half-reaction (conversion of p2 to v2) is faster in comparison to the second half-reaction (conversion of p4 to v4). The crystal structures and MD simulations both show significant differences in noncovalent interactions and flexibility of H118 between coproheme-*Cd*ChdC and MMD-*Cd*ChdC (Figures 3 and 4). In MMD-*Cd*ChdC p7 adapts a completely different position and loses interaction with H118. While the distance of H118 to the coproheme iron is relatively constant in all five subunits (0.4−0.6 nm), the residue is highly flexible, moving back and forth from the heme iron within 1.2 nm in the majority of the subunits in the MMD complex (Figure 5). A less stable conformation and higher flexibility of the catalytic H118 are likely to impair Compound I formation and decelerate the formation of heme *b* from MMD. Moreover, diminished interaction with p7 should result in decreased basicity of H118 in MMD-*Cd*ChdC in comparison to coproheme-*Cd*ChdC and consequently in a decreased rate of Compound I formation. This could be the reason we were not able to monitor a spectrum representative for MMD-Compound I (Figure 7A).

Summing up, our comprehensive biochemical and biophysical study on *Cd*ChdC allows us to propose the molecular mechanism of actinobacterial ChdCs, as illustrated in Figure 9. Due to the presence of H118 formation of Compound I and subsequently of Compound I* of clade 2, ChdCs are significantly faster in comparison to firmicute ChdCs. As a consequence, actinobacterial ChdCs exhibit a higher catalytic efficiency in heme *b* formation and are less prone to oxidative damage of the redox-active substrate. Coproheme-Compound I formation is faster in comparison to MMD-Compound I formation due to changes in noncovalent interactions of H118 after rotation of MMD. Clade 1 and 2 representatives seem to behave similarly with respect to the radical mechanism of decarboxylation of p2 by coproheme-Compound I* (oxoiron(IV) Y135$^{\bullet}$) and p4 by MMD-Compound I* (oxoiron(IV) Y135$^{\bullet}$) (Figure 9). Rotation of MMD by 90° after formation of the vinyl group at position 2, as proposed for firmicute ChdCs,[8,9] is supported by the first high-resolution crystal structure of an actinobacterial MMD-ChdC. However, the

https://dx.doi.org/10.1021/acscatal.0c00411
ACS Catal. 2020, 10, 5405−5418

mechanism of movement of MMD, e.g. whether it partially exits and re-enters the active site during rotation, is still unknown.

■ ASSOCIATED CONTENT

Supporting Information

The Supporting Information is available free of charge at https://pubs.acs.org/doi/10.1021/acscatal.0c00411.

Structural data and phylogeny of ChdCs, far- and near-UV circular dichroism spectra and HPLC-SEC-MALS data of recombinant wild-type (wt) *Cd*ChdC and variants, and comparison of *Cd*ChdC structures derived from X-ray crystallography and homology modeling (PDF)

■ AUTHOR INFORMATION

Corresponding Author

Stefan Hofbauer − *Department of Chemistry, Institute of Biochemistry, BOKU−University of Natural Resources and Life Sciences, A-1190 Vienna, Austria;* orcid.org/0000-0003-3375-7715; Phone: +43-1-47654-77258; Email: stefan.hofbauer@boku.ac.at; Fax: +43-1-47654-77059

Authors

Hanna Michlits − *Department of Chemistry, Institute of Biochemistry, BOKU−University of Natural Resources and Life Sciences, A-1190 Vienna, Austria*

Bettina Lier − *Department of Material Sciences and Process Engineering, Institute of Molecular Modeling and Simulation, BOKU−University of Natural Resources and Life Sciences, A-1190 Vienna, Austria*

Vera Pfanzagl − *Department of Chemistry, Institute of Biochemistry, BOKU−University of Natural Resources and Life Sciences, A-1190 Vienna, Austria*

Kristina Djinović-Carugo − *Department for Structural and Computational Biology, Max Perutz Laboratories, University of Vienna, A-1030 Vienna, Austria; Department of Biochemistry, Faculty of Chemistry and Chemical Technology, University of Ljubljana, 1000 Ljubljana, Slovenia;* orcid.org/0000-0003-0252-2972

Paul G. Furtmüller − *Department of Chemistry, Institute of Biochemistry, BOKU−University of Natural Resources and Life Sciences, A-1190 Vienna, Austria;* orcid.org/0000-0002-1199-2469

Chris Oostenbrink − *Department of Material Sciences and Process Engineering, Institute of Molecular Modeling and Simulation, BOKU−University of Natural Resources and Life Sciences, A-1190 Vienna, Austria;* orcid.org/0000-0002-4232-2556

Christian Obinger − *Department of Chemistry, Institute of Biochemistry, BOKU−University of Natural Resources and Life Sciences, A-1190 Vienna, Austria;* orcid.org/0000-0002-7133-3430

Complete contact information is available at: https://pubs.acs.org/10.1021/acscatal.0c00411

Notes

The authors declare no competing financial interest.

■ ACKNOWLEDGMENTS

This project was supported by EQ-BOKU VIBT GmbH and the BOKU Core Facility *Biomolecular & Cellular Analysis*. We thank Daniel Maresch for technical support in performing mass spectrometry analysis. This project was supported by the Austrian Science Fund, FWF project P29099, and FWF doctoral program BioToP (W1224). Data were collected at beamline ID29 of the European Synchrotron Radiation Facility (proposal MX1998).

■ ABBREVIATIONS

5cHS, five-coordinated high spin; 6cLS, six-coordinated low spin; *Cd*, *Corynebacterium diphtheriae*; ChdC, coproheme decarboxylase; CT, charge transfer; ECD, electronic circular dichroism; IPTG, isopropyl-*β*-D-thiogalactopyranoside; *Lm*, *Listeria monocytogenes*; MALS, multiangle light scattering; MD, molecular dynamics; MMD, monovinyl monopropionyl deuteroheme; p2, propionate at position 2; p4, propionate at position 4; p6, propionate at position 6; p7, propionate at position 7; *Sa*, *Staphylococcus aureus*; SEC, size exclusion chromatography; SPC, simple point charge; v2, vinyl at position 2

■ REFERENCES

(1) Dailey, H. A.; Dailey, T. A.; Gerdes, S.; Jahn, D.; Jahn, M.; O'Brian, M. R.; Warren, M. J. Prokaryotic Heme Biosynthesis: Multiple Pathways to a Common Essential Product. *Microbiol. Mol. Biol. Rev.* **2017**, *81*, No. e00048-16.

(2) Dailey, H. A.; Gerdes, S. HemQ: An Iron-Coproporphyrin Oxidative Decarboxylase for Protoheme Synthesis in Firmicutes and Actinobacteria. *Arch. Biochem. Biophys.* **2015**, *574*, 27−35.

(3) Pfanzagl, V.; Holcik, L.; Maresch, D.; Gorgone, G.; Michlits, H.; Furtmüller, P. G.; Hofbauer, S. Coproheme Decarboxylases - Phylogenetic Prediction Versus Biochemical Experiments. *Arch. Biochem. Biophys.* **2018**, *640*, 27−36.

(4) Dailey, H. A.; Gerdes, S.; Dailey, T. A.; Burch, J. S.; Phillips, J. D. Noncanonical Coproporphyrin-Dependent Bacterial Heme Biosynthesis Pathway that Does Not Use Protoporphyrin. *Proc. Natl. Acad. Sci. U. S. A.* **2015**, *112*, 2210−2215.

(5) Lobo, S. A.; Scott, A.; Videira, M. A.; Winpenny, D.; Gardner, M.; Palmer, M. J.; Schroeder, S.; Lawrence, A. D.; Parkinson, T.; Warren, M. J.; Saraiva, L. M. Staphylococcus aureus Haem Biosynthesis: Characterisation of the Enzymes Involved in Final Steps of the Pathway. *Mol. Microbiol.* **2015**, *97*, 472−487.

(6) Celis, A. I.; Streit, B. R.; Moraski, G. C.; Kant, R.; Lash, T. D.; Lukat-Rodgers, G. S.; Rodgers, K. R.; DuBois, J. L. Unusual Peroxide-Dependent, Heme-Transforming Reaction Catalyzed by HemQ. *Biochemistry* **2015**, *54*, 4022−32.

(7) Hofbauer, S.; Mlynek, G.; Milazzo, L.; Pühringer, D.; Maresch, D.; Schaffner, I.; Furtmüller, P. G.; Smulevich, G.; Djinovic-Carugo, K.; Obinger, C. Hydrogen Peroxide-Mediated Conversion of Coproheme to Heme b by HemQ - Lessons from the First Crystal Structure and Kinetic Studies. *FEBS J.* **2016**, *283*, 4386−4401.

(8) Streit, B. R.; Celis, A. I.; Moraski, G. C.; Shisler, K. A.; Shepard, E. M.; Rodgers, K. R.; Lukat-Rodgers, G. S.; DuBois, J. L. Decarboxylation Involving a Ferryl, Propionate, and a Tyrosyl Group in a Radical Relay Yields Heme *b*. *J. Biol. Chem.* **2018**, *293*, 3989−3999.

(9) Milazzo, L.; Gabler, T.; Pühringer, D.; Jandova, Z.; Maresch, D.; Michlits, H.; Pfanzagl, V.; Djinovic-Carugo, K.; Oostenbrink, C.; Furtmüller, P. G.; Obinger, C.; Smulevich, G.; Hofbauer, S. Redox Cofactor Rotates during Its Stepwise Decarboxylation: Molecular Mechanism of Conversion of Coproheme to Heme *b*. *ACS Catal.* **2019**, *9*, 6766−6782.

(10) Dailey, T. A.; Boynton, T. O.; Albetel, A. N.; Gerdes, S.; Johnson, M. K.; Dailey, H. A. Discovery and Characterization of

HemQ: an Essential Heme Biosynthetic Pathway Component. *J. Biol. Chem.* **2010**, *285*, 25978−25986.
(11) Hofbauer, S.; Hagmüller, A.; Schaffner, I.; Mlynek, G.; Krutzler, M.; Stadlmayr, G.; Pirker, K. F.; Obinger, C.; Daims, H.; Djinović-Carugo, K.; Furtmüller, P. G. Structure and Heme-Binding Properties of HemQ (Chlorite Dismutase-like Protein) from Listeria monocytogenes. *Arch. Biochem. Biophys.* **2015**, *574*, 36−48.
(12) Celis, A. I.; Gauss, G. H.; Streit, B. R.; Shisler, K.; Moraski, G. C.; Rodgers, K. R.; Lukat-Rodgers, G. S.; Peters, J. W.; DuBois, J. L. Structure-Based Mechanism for Oxidative Decarboxylation Reactions Mediated by Amino Acids and Heme Propionates in Coproheme Decarboxylase (HemQ). *J. Am. Chem. Soc.* **2017**, *139*, 1900−1911.
(13) Milazzo, L.; Hofbauer, S.; Howes, B. D.; Gabler, T.; Furtmüller, P. G.; Obinger, C.; Smulevich, G. Insights into the Active Site of Coproheme Decarboxylase from Listeria monocytogenes. *Biochemistry* **2018**, *57*, 2044−2057.
(14) Milazzo, L.; Gabler, T.; Pfanzagl, V.; Michlits, H.; Furtmüller, P. G.; Obinger, C.; Hofbauer, S.; Smulevich, G. The Hydrogen Bonding Network of Coproheme in Coproheme Decarboxylase from Listeria monocytogenes: Effect on Structure and Catalysis. *J. Inorg. Biochem.* **2019**, *195*, 61−70.
(15) Incardona, M. F.; Bourenkov, G. P.; Levik, K.; Pieritz, R. A.; Popov, A. N.; Svensson, O. EDNA: a Framework for Plugin-Based Applications Applied to X-Ray Experiment Online Data Analysis. *J. Synchrotron Radiat.* **2009**, *16*, 872−879.
(16) McCoy, A. J.; Grosse-Kunstleve, R. W.; Adams, P. D.; Winn, M. D.; Storoni, L. C.; Read, R. J. Phaser Crystallographic Software. *J. Appl. Crystallogr.* **2007**, *40*, 658−674.
(17) Adams, P. D.; Afonine, P. V.; Bunkóczi, G.; Chen, V. B.; Davis, I. W.; Echols, N.; Headd, J. J.; Hung, L. W.; Kapral, G. J.; Grosse-Kunstleve, R. W.; McCoy, A. J.; Moriarty, N. W.; Oeffner, R.; Read, R. J.; Richardson, D. C.; Richardson, J. S.; Terwilliger, T. C.; Zwart, P. H. PHENIX: a Comprehensive Python-Based System for Macromolecular Structure Solution. *Acta Crystallogr., Sect. D: Biol. Crystallogr.* **2010**, *66*, 213−221.
(18) Emsley, P.; Lohkamp, B.; Scott, W. G.; Cowtan, K. Features and Development of Coot. *Acta Crystallogr., Sect. D: Biol. Crystallogr.* **2010**, *66*, 486−501.
(19) Schmid, N.; Christ, C.; Christen, M.; Eichenberger, A.; van Gunsteren, W. Architecture, Implementation and Parallelisation of the GROMOS Software for Biomolecular Simulation. *Comput. Phys. Commun.* **2012**, *183*, 890−903.
(20) Reif, M. M.; Hünenberger, P. H.; Oostenbrink, C. New Interaction Parameters for Charged Amino Acid Side Chains in the GROMOS Force Field. *J. Chem. Theory Comput.* **2012**, *8*, 3705−3723.
(21) Zou, C.; Larisika, M.; Nagy, G.; Srajer, J.; Oostenbrink, C.; Chen, X.; Knoll, W.; Liedberg, B.; Nowak, C. Two-Dimensional Heterospectral Correlation Analysis of the Redox-Induced Conformational Transition in Cytochrome c Using Surface-Enhanced Raman and Infrared Absorption Spectroscopies on a Two-Layer Gold Surface. *J. Phys. Chem. B* **2013**, *117*, 9606−9614.
(22) Berendsen, H. J. C.; Postma, J. P. M.; van Gunsteren, W. F.; Hermans, J. *Interaction Models for Water in Relation to Protein Hydration*; Reidel: Dordrecht, The Netherlands, 1981; pp 331−342.
(23) Hockney, R. W. The Potential Calculation and Some Applications. *Methods Comput. Phys.* **1970**, *9*, 136−211.
(24) Ryckaert, J. P.; Ciccotti, G.; Berendsen, H. J. C. Numerical Integration of Cartesian Equations of Motion of a System with Constraints: Molecular Dynamics of n-Alkanes. *J. Comput. Phys.* **1977**, *23*, 327−341.
(25) Heinz, T. N.; van Gunsteren, W. F.; Hünenberger, P. H. Comparison of Four Methods to Compute the Dielectric Permittivity of Liquids from Molecular Dynamics Simulations. *J. Chem. Phys.* **2001**, *115*, 1125−1136.
(26) Berendsen, H. J. C.; Postma, J. P. M.; van Gunsteren, W. F.; DiNola, A.; Haak, J. R. Molecular-Dynamics with Coupling to an External Bath. *J. Chem. Phys.* **1984**, *81*, 3684−3690.
(27) Eichenberger, A. P.; Allison, J. R.; Dolenc, J.; Geerke, D. P.; Horta, B. A.; Meier, K.; Oostenbrink, C.; Schmid, N.; Steiner, D.; Wang, D.; van Gunsteren, W. F. GROMOS++ Software for the Analysis of Biomolecular Simulation Trajectories. *J. Chem. Theory Comput.* **2011**, *7*, 3379−3390.
(28) Hofbauer, S.; Dalla Sega, M.; Scheiblbrandner, S.; Jandova, Z.; Schaffner, I.; Mlynek, G.; Djinovic-Carugo, K.; Battistuzzi, G.; Furtmüller, P. G.; Oostenbrink, C.; Obinger, C. Chemistry and Molecular Dynamics Simulations of Heme b-HemQ and Coproheme-HemQ. *Biochemistry* **2016**, *55*, 5398−5412.
(29) Dunford, H. B.; Hewson, W. D. Effect of Mixed Solvents on the Formation of Horseradish Peroxidase Compound I. The Importance of Diffusion-Controlled Reactions. *Biochemistry* **1977**, *16*, 2949−2957.
(30) Poulos, T. L.; Freer, S. T.; Alden, R. A.; Edwards, S. L.; Skogland, U.; Takio, K.; Eriksson, B.; Xuong, N.; Yonetani, T.; Kraut, J. The Crystal Structure of Cytochrome c Peroxidase. *J. Biol. Chem.* **1980**, *255*, 575−580.
(31) Poulos, T. L.; Kraut, J. The Stereochemistry of Peroxidase Catalysis. *J. Biol. Chem.* **1980**, *255*, 8199−8205.

https://dx.doi.org/10.1021/acscatal.0c00411
ACS Catal. 2020, 10, 5405−5418